Enhanced stability and efficiency in inverted perovskite solar cells through graphene doping of PEDOT:PSS hole transport layer

C. Redondo-Obispo [a], T.S. Ripolles [a,*], S. Cortijo-Campos [b], A.L. Álvarez [a], E. Climent-Pascual [c], A. de Andrés [b], C. Coya [a,*]

[a] Escuela Técnica Superior de Ingeniería de Telecomunicación, Universidad Rey Juan Carlos, C/Tulipán s/n, 28933 Madrid, Spain
[b] Instituto de Ciencia de Materiales de Madrid, Consejo Superior de Investigaciones Científicas, C/ Sor Juana Inés de la Cruz 3, 28049 Madrid, Spain
[c] Escuela Técnica Superior de Ingeniería Industrial, Universidad Politécnica de Madrid, C/ José Gutiérrez Abascal 2, 28006 Madrid, Spain

HIGHLIGHTS

- Addition of graphene platelets into PEDOT:PSS layers improves up to 10 times its conductivity, maintaining the transmittance.
- MAPbI$_3$ film grown on graphene-doped PEDOT:PSS exhibits large crystallite size and lower PbI2 content, leading high stability.
- Inverted solar cells based on graphene-doped PEDOT:PSS show better photovoltaic parameters by increasing charge extraction.

GRAPHICAL ABSTRACT
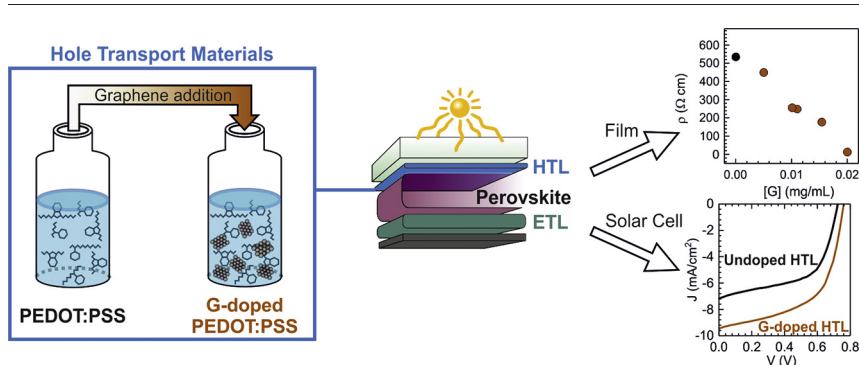
ARTICLE INFO

ABSTRACT

Poly(3,4-ethylenedioxythiophene):poly (styrene sulfonate) (PEDOT:PSS) plays a relevant role in the device performance as hole extraction layer (HTL) of inverted perovskite solar cells. Here, we show a simple low-temperature spin coating method for obtaining homogenous graphene-doped thin films of PEDOT:PSS with improved electrical conductivity without decreasing optical transmittance. Moreover, the crystallinity and stability in ambient conditions of the perovskite grown on it are enhanced. The hydrophobic character of graphene probably blocks undesirable reactions hampering degradation. By impedance spectroscopy it is demonstrated better charge extraction and reduction of recombination mechanisms at the doped-HTL/perovskite interface, resulting in improved photovoltaic parameters of the solar cell and greater stability at room operation conditions thus providing a simple and cost-effective method of preparing solar cells based on hybrid perovskites.

* Corresponding authors.
E-mail addresses: teresa.ripolles@urjc.es (T.S. Ripolles), carmen.coya@urjc.es (C. Coya).

1. Introduction

Hybrid organic-inorganic perovskite-based solar cells (PSCs) have reached similar efficiencies in recent years to commercial CdTe and $CuI_{1-x}Ga_xSe_2$ (CIGS) solar cells, with verified power conversion efficiencies (PCEs) as high as 24.2% within few years of their emergence [1]. This technology becomes very competitive due to the advantage of enabling cost-effective and low temperature processing, such as spin coating and printing. A PSC consists of a sandwich structure of transparent rigid or flexible substrate, an electron–selective (or hole–selective) electrode, followed by the metal halide perovskite and finishing with the hole transport layer (HTL) (or electron transport layer (ETL)) for the regular (or inverted) structures. The electron–selective electrodes may have mesoscopic or n-i-p configurations and the hole selective ones a p-i-n configuration [2–4]. It is known that the crystalline growth of hybrid perovskites, among other properties, is influenced by the nature of the underneath layer [5,6], being those regular solar cells with higher efficiencies [7]. The standard inverted PSCs is based on poly(3,4-ethylenedioxythiophene):poly (styrene sulfonate) (PEDOT:PSS) as HTL and its synthesis requires low fabrication costs, simple and solution processing techniques at low temperature (<150 °C), being suitable for flexible devices [8,9]. Nevertheless, PEDOT:PSS is not considered as the most efficient and appropriate HTL. One of the main challenges is the stability of these devices, which currently limits their practical applications and commercialization. The hygroscopic and acidic nature of PEDOT:PSS is an additional factor for the degradation of the active layer film. On the one hand, the absorbed water favours the decomposition of the perovskite and, on the other hand, the acidic nature of PSS- degrades the ITO (indium tin oxide) electrode, reacting with In_2O_3 dissociating indium ions, which also can easily diffuse into the active layer, further reducing the stability of the devices [10,11]. Besides, PEDOT:PSS conductivity, affected by the insulating character of PSS- group, is lower than the common ETL conductivity such as [6,6]- phenyl-C61-butyric acid methyl ester ($PC_{61}BM$). This difference in the charge-extraction-layer conductivity can cause photo-carrier losses and unbalanced charge transport in the device. In this case, the produced charge accumulation can reduce shunt resistance and fill factor (FF) and enhance leakage current [12,13].

The conductivity of the PEDOT:PSS layer depends on the arrangement and the amount of PEDOT- and PSS- groups. Among the methods used to modify the PEDOT:PSS properties, mainly conductivity, as HTL for inverted solar cells, are either solvent additives or solvent post-treatments [14,15]. For example, adding dimethyl sulfoxide (DMSO) [16,17] or rinsing the HTL with methanol (MeOH) and *N,N*-dimethylformamide (DMF) [18] leads to more efficient PSCs. However, conductivity is not the only factor to consider. For instance, the treatment of PEDOT:PSS with ethylene glycol (EG) produces higher conductivity values, but the efficiency of PSC is reduced, as a result of increasing the roughness of the layer that is associated with defects or traps that facilitate the recombination of the surface charge carriers achieving lower open circuit voltage (V_{OC}) and FF [19]. Morphology, roughness and crystallite size are important as well in order to facilitate an interfacial contact between the HTL and the perovskite layer allowing high V_{OC} and FF.

Recently, using composites or doping with graphene-related materials are other ways of modifying the properties of PEDOT:PSS HTL aimed at improving the efficiency of PSCs [20]. Graphene (G) and its derivatives such as graphene oxide (GO) or reduced graphene oxide (rGO) have been widely employed as additives in optoelectronic devices to improve electrical, optical and morphological properties [21–25]. Adding GO in the PEDOT:PSS layer, by composition or replacement of the HTL, has been intensively studied in inverted PSC with high efficiencies [26]. But, in spite of promising photovoltaic performance using PEDOT:PSS:GO composites, it should be noted that GO is an insulator due to the presence of oxygen containing functional groups on the carbon basal plane and, therefore, a precise control of the HTL thickness and/or GO concentration is necessary. An alternative has been approached through reduction processes that lead to more conductive rGO [27,28] but scarce works have been reported combining pristine graphene flakes with PEDOT:PSS. One reason may be the technological challenge of obtaining uniforms thin films due mainly to the hydrophobic character of graphene [29]. But it is this last property that could work as an excellent barrier to protect the solar cell absorber materials from unwanted chemical reactions. In addition, the extraordinary charge carrier mobility [30], exceptional thermal and chemical stability [31], and the great bridging potential between the PEDOT:PSS polymer segments, which favours stability in vibration-assisted spray coating PEDOT:PSS with graphene thin films [32], make graphene an ideal candidate to further studies. The commonly used PEDOT:PSS layer doped with graphene flakes as HTL in inverted perovskite solar cells has been scarcely explored yet, despite it has been studied in other fields, such as dye-sensitized solar cells [33], organic solar cells [34], flexible substrates [35], OLEDs [36], batteries [37], and microelectrodes [38].

In this work, few-layer graphene platelets are homogeneously incorporated into the PEDOT:PSS layers to partly fix the previously described drawbacks of this HTL when used in solar cell devices based on halide perovskites, taking advantage of the high conductivity and hydrophobicity of pristine graphene. Very low graphene concentrations in the precursor solutions (up to 0.02 mg/mL), well below graphene percolation threshold, are enough to increase the conductivity one order of magnitude without modifying the optical transmittance, which is a relevant factor to increase the device operation parameters. However, the most relevant impact is related to the perovskite layer itself. The morphology and surface character of the graphene-doped PEDOT:PSS layer induces an increase of the perovskite crystallite size, of its stability in ambient conditions with time and of the HTL/perovskite interfacial properties with better carrier extraction. We explore the photovoltaic performance under illumination for the solar cells with structure of ITO/G-doped PEDOT:PSS/MAPbI$_3$/PCBM/Al. The photovoltaic performance of the resulting cells was improved due to better charge extraction and reduction of recombination mechanisms at the interface of doped-HTL/perovskite characterized by impedance spectroscopy. These interrelated characteristics finally provide simple and low-temperature method to fabricate perovskite solar cells based on this proposed graphene-doped HTL paving the way to develop efficient flexible optoelectronic devices.

2. Experimental section

2.1. Materials

All materials were reagent grade and were used as received. PEDOT:PSS Clevious P VP AI 4083 aqueous solution from Heraeus. Pristine exfoliated graphene flakes suspension in THF (0.1 mg/mL) from GRAnPH Nanotech [39].

The standard perovskite absorber layer was $CH_3NH_3PbI_3$, MAPbI$_3$, synthetized by a stoichiometric mixture of iodine precursors (methylammonium iodide, MAI from Dyesol and lead iodide, PbI$_2$ from Aldrich (99.999%)). The anhydrous solvents used were DMSO (>99.8%) for the perovskite solution and toluene (99.8%) as antisolvent, both from Alfa Aesar. The electron transport material was a fullerene derivative PCBM (>99%, Aldrich), with anhydrous chlorobenzene (99.8%, Aldrich) as solvent.

Graphene-doped PEDOT:PSS thin films were prepared by a mixture of PEDOT:PSS with graphene suspension with the following concentrations, 0 mg/mL, 0.005 mg/mL, 0.01 mg/mL, 0.015 mg/mL, and 0.02 mg/mL, named as 0G, 0.005G, 0.01G, 0.015G and 0.02G, for simplifying. Each solution was sonicated for 5 min and maintained at 70 °C with the substrate before being spin coated at 2000 rpm for 45 s. Then, the layer was heated for 30 min at 120 °C in a hot plate.

2.2. Fabrication of solar cells

Solar cells with inverted planar structure: glass/ITO/PEDOT:PSS:G/MAPbI$_3$/PCBM/Yb/Al were prepared. Pre-pattern ITO on glass substrates (2.5 cm × 3 cm, 15 Ω/sq., from Lumtech Tech.) were cleaned by ultrasonic bath with acetone, and 2-propanol for 15 min, sequentially, and then blow-dried with N$_2$ gun. Before depositing the hole transport layer (HTL), an ultraviolet-ozone treatment for 12 min was carried out. After this surface treatment, all substrates were transferred to glove box up to the end of the experimental procedure. HTL was fabricated in the same conditions as described above. The precursor solution of MAPbI$_3$ (45 wt%) was prepared by mixing PbI$_2$ and MAI in DMSO. The solution was filtered by 0.2 μm hydrophilic polytetrafluoroethylene (PTFE) syringe filter prior to deposition. Solution and substrates were heated at 80 °C during the deposition process. A two steps spin coating method is used: 1000 rpm for 10 s, and 5000 rpm for 30 s. At 20 s of the second step, 500 μL of toluene was added. Immediately after coating process finished, substrates were transferred onto a hot plate at 100 °C for 60 min. At room temperature, 20 mg/mL of PCBM solution in chlorobenzene was deposited by spin coating at 2000 rpm for 40 s. Finally, for the metal electrode, Yb/Al were thermally evaporated through a shadow mask at 3 10^{-6} Torr. The device area was 25 mm^2, as defined by the overlap between the Al top electrode and the patterned ITO. The layer thicknesses were measured using an Alpha step 200 profilometry (Tenkor Instruments).

2.3. Methods

2.3.1. Cyclic voltammetry measurements

Electrochemical measurements of solutions were performed on an AUTOLAB PGSTAT302N at room temperature. The undoped- and doped-PEDOT:PSS solutions were analyzed at a scan rate of 100 mV/s in a conventional three-electrode configuration, glassy carbon electrode, Pt wire, and Ag/AgCl (KCl 3.5 M), as the working electrode, counter electrode, and reference electrode, respectively. Glassy carbon electrodes were polished with alumina.

2.3.2. Morphological characterization

Atomic force microscopy (AFM) topography images of undoped and graphene doped PEDOT:PSS films were done using an equipment and software from Nanotec™ in the tapping mode. Commercial tips (Nanosensors PPP-NCH-w) with k = 34 Nm^{-1} and f$_0$ ≈ 270 kHz were used. Morphology of the MAPbI$_3$ thin films on the different HTL layers were inspected by secondary electron images recorded using a Fei Inspect Scanning Electron Microscope (SEM) with an acceleration voltage of 15 kV.

The x-ray diffraction (XRD) diffractograms of the MAPbI$_3$ thin films were measured by Rigaku diffractometer using Cu Kα radiation over a 2θ range between 10° and 35° with a step size of 0.02°. To obtain the crystallite size, the FWHM data corresponding to reflections [121], [022] and [220] have been used, since they are not overlapped with other perovskite nor with the spurious phase. The experimental distribution is corrected with the extension of a "reference" (calcite), which has a maximum in 23° in 2θ.

2.3.3. Optical characterization

For the optical characterization, UV-VIS absorption or transmittance spectra of the thin films were characterized using a UV-VIS-NIR spectrophotometer (Varian, Cary 500) in the wavelength range of 300–900 nm. Steady state photoluminescence emission (PL) of the films were carried out in the visible 400–900 nm range measurements using a high sensitivity fiber optic AVANTES spectrometer, model AvaSpec-HERO (100 mm optical bench), NA of 0.13 and a Peltier cooled, back-thinned detector (1024 × 58 pixels) and a 30 mm integrating sphere (250–2500 nm) AvaSphere-30-REFL. The excitation wavelength was 360 nm (10 mW) of a solid state fiber-coupled laser (CNILASER).

Micro-Raman spectra of graphene flakes were carried out using the 488 nm excitation wavelength of an Ar$^+$ laser in backscattering geometry with an Olympus microscope, a "super-notch-plus" Filter from Kaiser and a Jobin-Yvon HR-460 monochromator coupled to a Peltier cooled Synapse CCD.

2.3.4. Electrical characterization

All measurements were carried out in ambient conditions at 298 K and <30% of RH. Resistivity of the doped-PEDOT:PSS thin films were measured by means of four-point probing system in 2.5 mm apart silver paint contacts. The perovskite solar cells (PSCs) were kept in dark and N$_2$ atmosphere in the intermediate time periods. The current-voltage (J-V) curves of the solar cells were measured in forward and reverse scans using a Keithley 2450 sourcemeter under AM 1.5G (100 mW/cm^2) provided by a LED solar simulator SINUS-70 (Spectral match class A+++) from WAVELABS, with reference intensity sensor in test plane in combination with fast feedback loop for automatic intensity correction and temperature control for the LEDs. A black mask with apertures from 16 to 20 mm^2 are used to define the active area. The scan rate was 91 mV/s.

The impedance spectroscopy (IS) was measured using a Potentiostat Autolab-PGSTAT204 in a range of voltages, from short circuit to open circuit, with a step voltage of 50 mV. For each polarization point, an AC 20 mV voltage perturbation from 1 MHz to 100 mHz. Nova software was used to generate data and Z-View software for modelling the equivalent circuit model was used to fit the spectra.

3. Results and discussion

3.1. Graphene-doped PEDOT:PSS films

Raman spectra of graphene platelets correspond to few-layer graphene (Fig. 1a) with defects, mainly related to domain size. The narrow widths of G and 2D peaks reveal the superior quality of this graphene [40] compared to GO and rGO materials used in other works. [21–28] The thickness of the films increases <15%, from 65 to 75 nm, for the maximum graphene content (Fig. 1b). Additionally, a small increase (<13%) in the root-mean-square (rms) roughness is detected in the AFM images (rms roughness is 0.64 nm for the undoped film and 0.73 nm for that with maximum G content, Fig. 1c and f) in parallel, and most probably linked, to the thickening of the films. Slightly increased surface roughness could increase the contact area with the perovskite layer and results in more favourable charge extraction [41]. Graphene Raman modes are not detected in the films due to the low graphene content and to the coincidence in the frequency ranges with PEDOT:PSS vibrations.

Graphene introduction into the PEDOT:PSS HTL layer does not impair its optical transparency (Fig. 1d). Moreover, in-plane electrical resistivity, ρ, (Fig. 1e) obtained from current-voltage curves (Fig. S1), decreases with the addition of graphene up to one order of magnitude for 0.02G film compared to that of undoped PEDOT:PSS film. This behaviour may be attributed to the appropriate energy-level matching between graphene and PEDOT:PSS and a final homogeneous distribution of graphene into the HTL layer. Increasing the conductivity of the HTL film is very relevant since it can lead to a decrease in series resistance (R$_s$) thus enhancing charge collection efficiency [42].

To clarify the contribution of graphene content on the work function of PEDOT:PSS, cyclic voltammetry (CV) was measured to determine the highest occupied molecular orbital (HOMO) level of PEDOT:PSS and G-PEDOT:PSS solutions (see SI for experimental details). From the obtained voltammograms (Fig. S2), the oxidation potentials have been extracted indicating very similar HOMO energy levels of 5.34, 5.34, 5.35, 5.36 and 5.32 eV for 0G, 0.01G, 0.015G and 0.02G solutions respectively (5.3 eV is a commonly reported value for PEDOT:PSS) [2,10]. Thus, such concentrations of graphene have no appreciable influence on the HOMO level of the doped HTL.
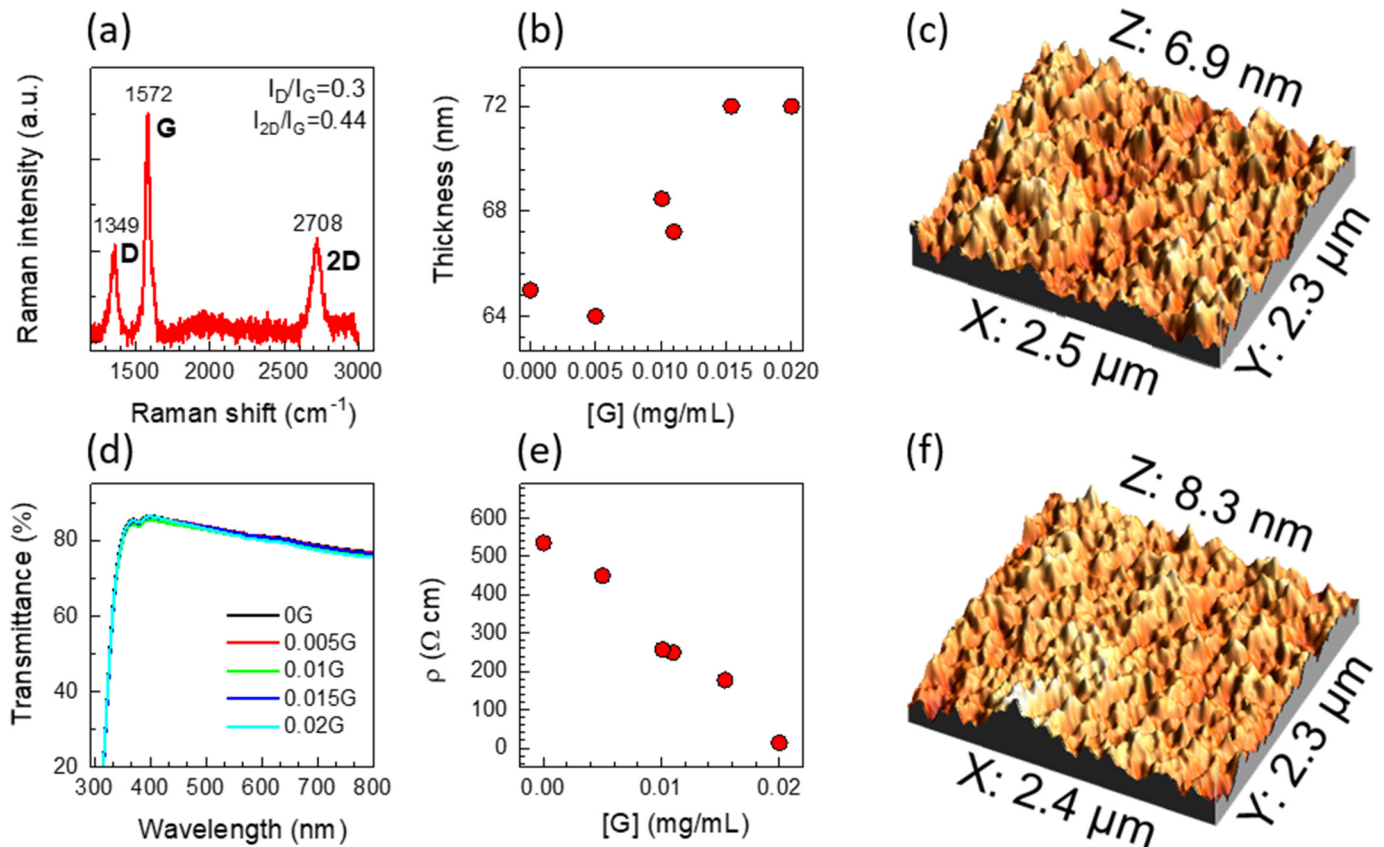
Fig. 1. (a) Raman spectra of graphene flakes from GRAnPH Nanotech dispersed in THF. (b) Thickness, (d) optical transmittance and (e) electrical resistivity of undoped and G-doped PEDOT:PSS films. (c) and (f) AFM topographic images of 0G and 0.02G films.

3.2. Effect on the perovskite layer: morphology and crystalline structure

SEM images of the standard perovskite MAPbI$_3$ films deposited on the different G-doped PEDOT:PSS layers show similar morphology (Fig. S3). The overall measured thickness by contact profilometry is 428 nm for the MAPbI$_3$ on glass and varies around 10% for those deposited on the graphene doped PEDOT:PSS layers: 490, 463, 473, 480 and 500 nm on 0G, 0.005G, 0.01G, 0.015G and 0.02G, respectively.

It has been shown that the preferential orientation and the interfacial properties of the perovskite MAPbI$_3$ thin film depend directly on the nature of the substrate [5]. To evaluate the possible impact of the introduction of graphene into the HTL, structural XRD characterization was performed for MAPbI$_3$ films grown on these different G-doped PEDOT:PSS layers. XRD patterns of the pristine MAPbI$_3$ (Fig. 2a) correspond to the non-centrosymmetric I4 cm space group, considering a polar tetragonal structural model, where the C—N bonds of the methylammonium cations are fixed parallel to the c-axis [43]. The films display preferential orientation in the [110] direction around 25%, as reported previously for MAPbI$_3$ grown on PEDOT:PSS [5], and does not change significantly with the presence of graphene. Interestingly, the crystallite size perpendicular to the substrate of the [110] grains, calculated from Scherrer equation for the [220] peak, increases >40% for MAPbI$_3$ films on 0.015G PEDOT and the crystal size for the polycrystalline grains increases >70%, obtained from [121] and [022] diffraction peaks (Fig. 2b).

The XRD patterns also reveal a small contribution of PbI$_2$, commonly observed in MAPbI$_3$ films, assigned to the [001] reflection, at 12.6°, of the hexagonal PbI$_2$ [44]. Interestingly, the biggest contribution of PbI$_2$ corresponds to undoped PEDOT:PSS while the presence of graphene into the HTL layer clearly inhibits the formation of PbI$_2$ (Fig. S4). Several degradation routes are associated to PEDOT:PSS film: the acidic and hygroscopic nature of this HTL material promotes the degradation of ITO and MAPbI$_3$ layers [10]. Additionally, some reactions with residual moisture trapped in the structure, most likely derived from the water dispersion of PEDOT:PSS, lead to the decomposition of the perovskite too [11]. Here, however, the introduction of a small fraction of graphene in the PEDOT:PSS HTL layer significantly reduces the formation of PbI$_2$ when the perovskite layer is grown on top of it. Fig. 2c shows the ratio between PbI$_2$ [001] reflection at 12.6° and MAPbI$_3$ [110] reflection at 14.2° in as grown samples as well as its evolution in ambient conditions (298 K) for 576 h after the thin films were irradiated for 2 h under AM 1.5G (100 mW/cm^2). This ratio is always lower for MAPbI$_3$ deposited on G-doped PEDOT:PSS. XRD patterns of aged samples, after illumination for 2 h under AM 1.5G (100 mW/cm^2) in ambient conditions (298 K) are shown in Fig. S4b.

3.3. Effect on perovskite layer: Optical absorption and photoluminescence

Optical absorption spectra of MAPbI$_3$ thin films deposited on glass as a reference, PEDOT:PSS and G-PEDOT:PSS layers are presented in Fig. 3a. These spectra correspond well with previously published results for MAPbI$_3$, with absorption coefficients around 10^5 cm^{-1} and sharp optical absorption edges [45]. The minima of the second derivatives indicate with precision the optical transition energies (inset of Fig. 3a) [46,47]. One local minima is observed at 775 nm (1.6 eV $\pm$ 0.05 eV) for all films (the full width at half-maximum of the second derivative is assumed as the error) that corresponds to the direct semiconductor-type transitions at the R point in the pseudo-cubic Brillouin zone [45,48]. Thus, as expected, the introduction of pristine graphene in the PEDOT:PSS HTL layer does not induce changes in the band gap energy, E$_g$, of the MAPbI$_3$ grown on it. The extent of the absorption tail below the band gap is intimately associated with the degree of energetic
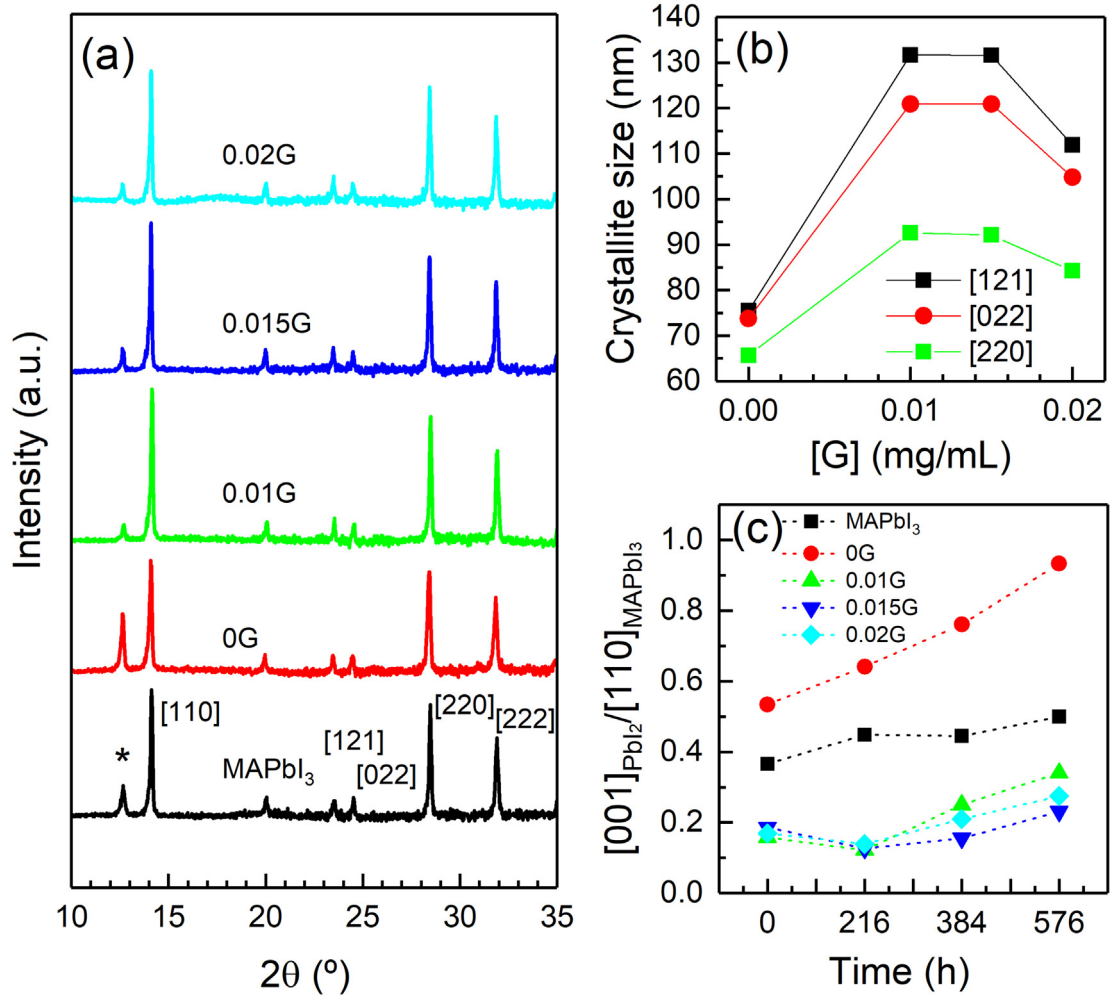
Fig. 2. XRD (Cu K$_{\alpha1/\alpha2}$) patterns of the (a) pristine MAPbI$_3$ films on glass and on 0G, 0.01G, 0.015G and 0.02G PEDOT:PSS layers (* corresponds to PbI$_2$ [001] reflection); (b) crystallite size calculated by Scherrer equation at [121], [022] and [220] reflection peaks; and (c) time evolution of the integrated area ratio of PbI$_2$ [001] reflection at 12.6° and MAPbI$_3$ [110] reflection at 14.2°.

disorder within the material, which stems from thermal fluctuations of the ions comprising the material or from defects in the perovskite structure. This energetic disorder can be characterized by the Urbach energy

E_U [49], assuming that below the band gap energy, i.e. 1.6 eV, the absorption follows an exponential trend: $\alpha \sim \exp.(h\nu/E_U)$. G-doping does not induce significant changes on E_U, obtaining values slightly above
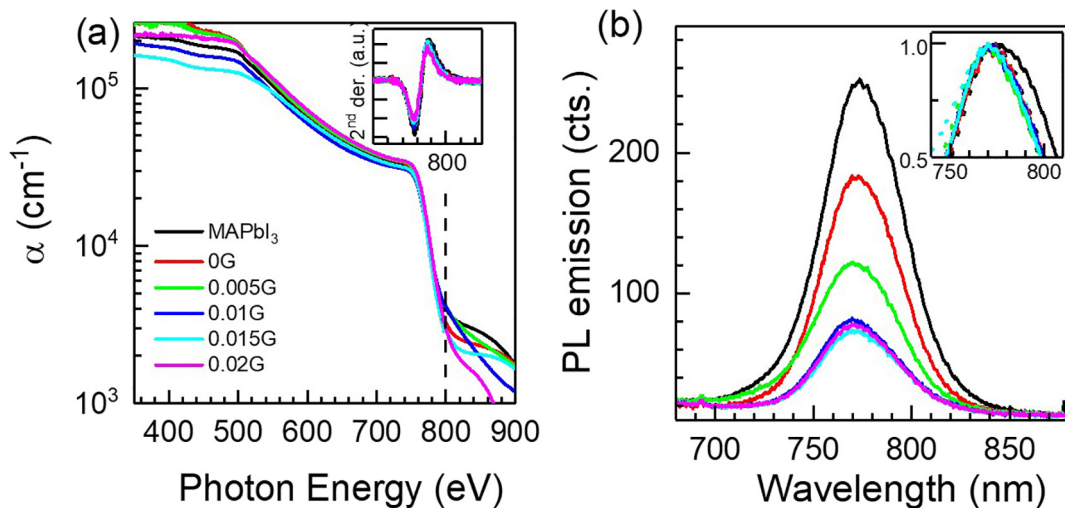

Fig. 3. (a) Absorption spectra and (b) steady PL emission ($\lambda_{exc} = 360$ nm) of MAPbI$_3$ thin films deposited on glass, PEDOT:PSS and PEDOT:PSS doped with graphene: 0G to 0.02G. The insets show (a) the second derivative in the 700–850 nm wavelength range showing the minima at 770 nm, and (b) zoom of maximum normalized PL spectra.

those obtained for the highest quality MAPbI$_3$ thin films (15 meV): [50] 31, 34, 31, 35, 38 and 32 meV for 0G to 0.02G samples and MAPbI$_3$ on glass (Fig. S5).

Steady PL emission of the films was measured under UV excitation (360 nm, 10 mW) using an integrating sphere in order to compare all measurements. Since these materials present a light soaking effect in ambient conditions, which is an initial increase in luminescence intensity over minutes under illumination [5,51], Fig. 3b shows PL spectra obtained by averaging several measurements once the emission is stabilized. MAPbI$_3$ thin film on glass exhibit the characteristic maximum at 775 nm while all MAPbI$_3$ thin films on graphene-doped HTL display a slightly blue-shifted PL peak at 770 nm (inset of Fig. 3b). Compared to the PL emission of the MAPbI$_3$ layer on glass, the PL intensity of the perovskite film on 0G-PEDOT:PSS layer decreases by about 30%, and the addition of graphene induces an additional decrease of about 30%. PL quenching may be due either to an increased number of traps in the MAPbI$_3$ layer or to longer exciton lifetime, related to the reduction of grain boundaries density that, conversely, could increase the non-radiative recombination probability at the interfaces with the charge transporting layers in open circuit conditions. The results in the devices shown below point to the second option, which supports that the presence of small graphene content in the PEDOT:PSS HTL layer induces better charge extraction capability in operation and, therefore, more favourable interfacial properties.

Moreover, after 1 h illumination (AM 1.5G in ambient conditions at 298 K) the PL emission of the MAPbI$_3$ on G-PEDOT:PSS remains stable whereas the emission intensity of MAPbI$_3$ on undoped-PEDOT:PSS keeps evolving (Fig. S6), what is compatible with mayor content of

non-passivated traps [52], which is unfavourable for charge carrier collection [53,54].

3.4. Photovoltaic characteristics

To study the influence of graphene addition to PEDOT:PSS on photovoltaic devices, solar cells with inverted p-i-n structures were fabricated (Fig. 4a) according to the method described in the SI. An energy levels diagram is shown in Fig. 4b. The current-voltage curves, J-V, of the PSCs under AM 1.5G illumination are shown in Fig. 4c. Such small graphene contents in the HTL layer induce relevant improvements in the photovoltaic parameters (Fig. S7), in particular, 0.02G HTL device increases up to 38%, 5.6% and 33%, short current density J$_{SC}$, open circuit voltage V$_{OC}$, and photoconversion efficiency PCE, respectively. This is most probably induced, on the one hand, by the larger MAPbI$_3$ crystallite size for the graphene-HTL devices, which reduces the grain boundary density and therefore a smaller number of recombination centers are present [55], and, on the other hand, the increment of conductivity for graphene-doped PEDOT:PSS that enhances the charge collection efficiency.

The effect of a higher electrical conductivity of the HTL layer with the addition of graphene can also be noticed in the characteristic J-V curves in dark conditions (Fig. 4d), as a small increment in the current density below the voltage threshold, which has an effect in the FF. Fig. S7 shows the evolution of FF with graphene content, and although it initially decreases slightly, it increases for the 0.02G HTL layer device and does not worsen the efficiency in any case. Further, as mentioned above, the conductivity increment of the HTL films can lead to a decrease in
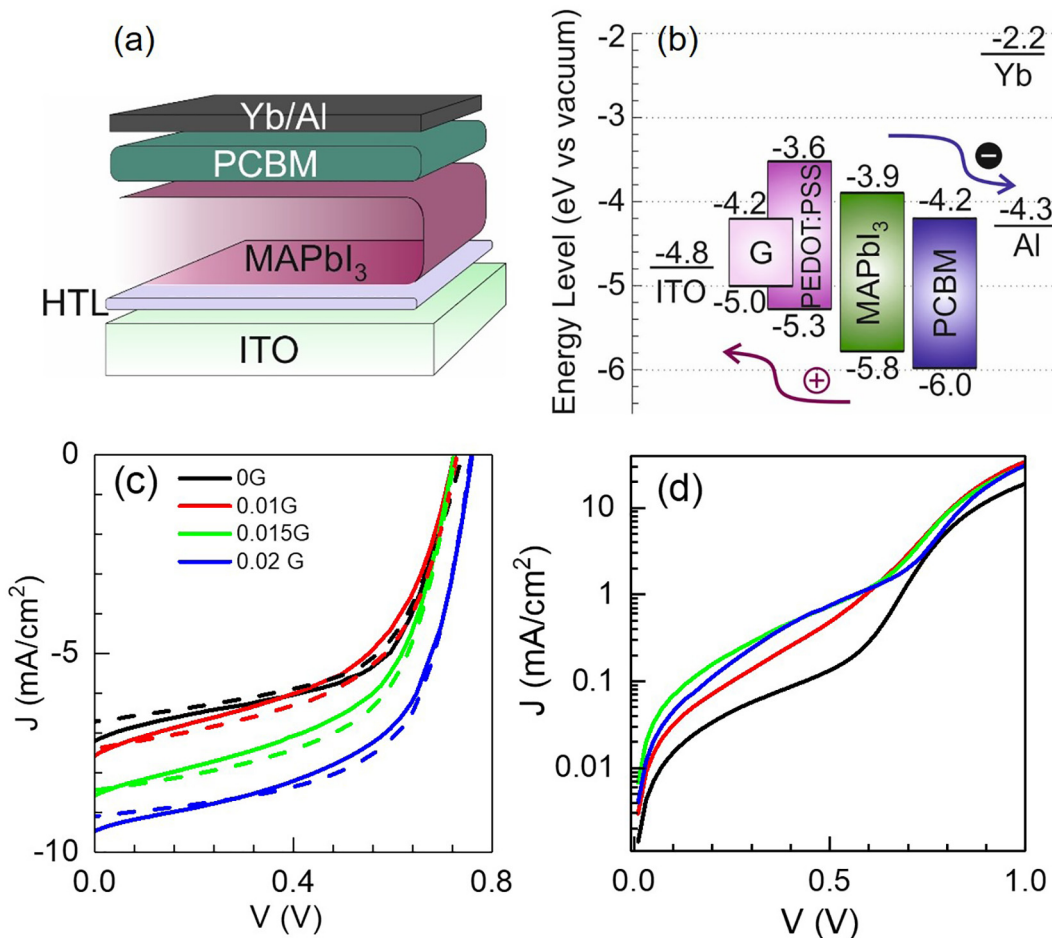

Fig. 4. (a) Layer structure of the inverted solar cell, (b) energy levels diagram, [2,10] (c) current-voltage performances under 1 sun illumination for the solar cells based on 0G, 0.005G, 0.01G, 0.015G and 0.02G as HTL in forward sweep (solid lines) and reverse sweep (dashed lines), and (d) current-voltage curves under dark conditions.

series resistance (R_s) thus enhancing the charge collection efficiency [42]. Regarding V_{OC}, an improvement could be related with a better energy level alignment between the valence band of the MAPbI$_3$ and the HOMO level of the graphene-doped HTL layer. But, since our voltammetry measurements do not show significant changes induced by graphene content it should be related with a decreasing leakage current as observed in previous works when doping the PEDOT:PSS layer with graphene oxide (GO) and also with small molecules [24,56].

3.5. Impedance spectroscopy

To further investigate the different processes caused by the modification of the HTL layer in an inverted perovskite solar cell, the devices were analyzed by IS under a constant illumination with AM 1.5G (100 mW/cm^2). IS has been demonstrated as a useful technique to investigate the operation principles of photovoltaic devices [57,58], including PSCs [59,60]. IS enables detailed information about internal processes in the devices under various operation conditions [60,61]. Here, IS measurements were carried out using a voltage perturbation of V_{AC} of 20 mV in the frequency range from 1 MHz to 0.1 Hz at each polarization voltage, V_{DC}, from short circuit to close open circuit conditions, every 50 mV (more details in the SI). This technique distinguishes between different processes, each mechanism occurs at a specific time scale, being slow lifetimes characteristic of ionic processes, either in the bulk or at interfaces, and fast lifetimes characteristic to pure electrical processes [62]. Each process is associated with a resistance and capacitance pair coupled in parallel.

A proper interpretation of the impedance spectra requires to decide a suitable equivalent circuit model to fit the experimental data (capacitance and impedance spectra in Fig. S8). The literature offers a large

variety of models and currently it is a matter of debate in solar cells based on perovskites [62–64].

High efficient PSCs are commonly fitted with an equivalent circuit model (Fig. 5a) which separates only two characteristic times, at low (LF) and high (HF) frequency regimes, associated to $R_{LF}\|C_{LF}$ and $R_{HF}\|C_g$ each. However, the impedance spectra showed in Fig. 5c–f presents a new element. In particular, the large semicircle is fitted with resistance and capacitance values, defined as $R_{LF}\|C_{LF}$, at LF range; and the small semicircle fits properly with the combination of $R_{HF}\|C_g$ at HF range and a third pair $R_{IF}\|C_{IF}$ at intermediate frequency range (IF) [65], despite the effect of $R_{IF}\|C_{IF}$ is not detected in the capacitance spectra (Fig. S8a). Therefore, there are two mechanisms intertwined at HF and IF regimes and, in order to fit properly these spectra (Fig. S8b), three different processes must be considered (LF, IF and HF). The equivalent circuit model used is represented in Fig. 5b. The appearance of another process in the IF region in all PSCs is indicative of non-optimized devices as in the present case. Bearing these considerations in mind, the experimental data were fitted (Fig. 5) and significant parameters were extracted at the three frequency regimes (Figs. S9 and 6). These parameters are corrected by the DC current and the series resistance, $V_d = V_{app} - V_s$, being V_{app} and V_d the applied and the device potential, respectively.

According to this analysis, the capacitance at HF domain (Fig. S9a) C_g (called geometrical capacitance) depends mainly on the bulk perovskite layer, in this case MAPbI$_3$ is found to be independent of the applied voltage with a constant value of $68.6 \cdot nF \, cm^{-2}$ in correspondence with other reported values [64].

It is interesting to note that at low and high frequencies regimes, R and C parameters behave independently of the amount of G added in the HTL layer (see Fig. S9). Conversely, the equivalent parameters at intermediate regime are influenced by G content (Fig. 6a). Close to short
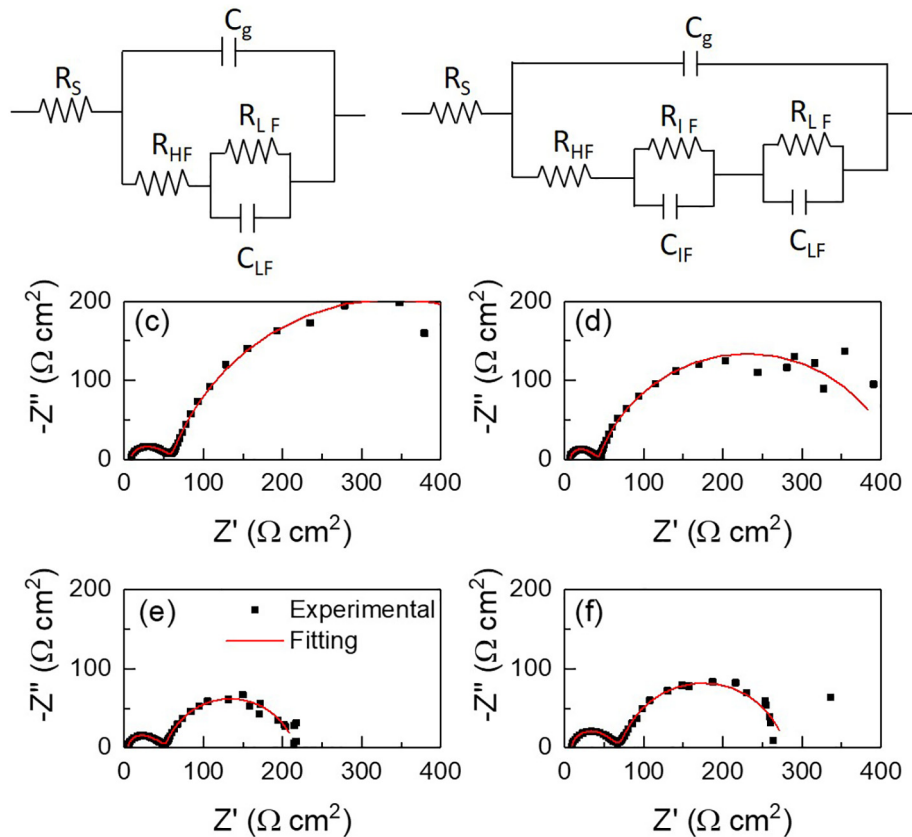

Fig. 5. Equivalent circuit models for (a) high efficient solar cells and (b) solar cells characterized by electrical mechanisms with loss of charge. The equivalent circuit model in (b) fitted the impedance spectra at short circuit conditions under light for all devices under study, 0 (a), 0.01 (b), 0.015 (c), and 0.02 (d) mg/mL of graphene in the PEDOT:PSS layer in inverted perovskite solar cells. Solid line corresponds to fitting results.
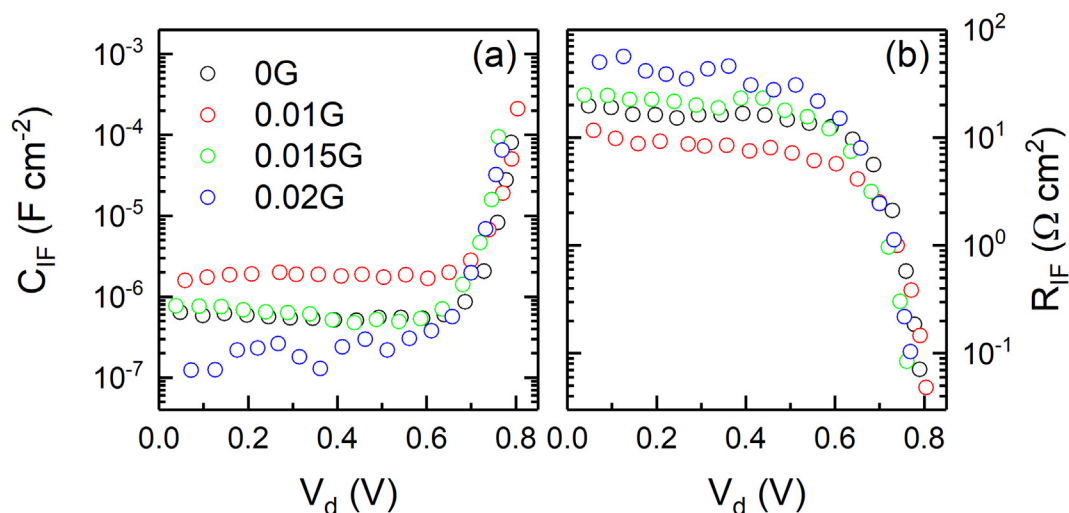
Fig. 6. Capacitive (a) and resistive (b) elements at IF domain under light for inverted perovskite solar cells with standard, 0G, and 0.01G, 0.015G, and 0.02G graphene doped HTL layers. The plots are corrected to the device voltage, V_d, due to voltage drop of resistance processes.

circuit DC voltages, capacitance C_{IF} becomes constant, $5.7 \cdot 10^{-7}$, $1.8 \cdot 10^{-6}$, $6.2 \cdot 10^{-7}$, and $2.1 \cdot 10^{-7}$ Fcm^{-2} for 0G, 0.01G, 0.015G, and 0.02G, respectively. The addition of 0.02 mg/mL of graphene into the PEDOT:PSS, reduces the capacitance C_{IF} substantially, reaching very low values. This is consistent with a reduction in the charge accumulation at the interface reflected in the increased photovoltaic performance (Fig. 4c). Additionally, the device with 0.01G film showed an increment in the C_{IF}, meaning that such small doping affects the charge extraction mechanism. Additionally, the charge extraction process at interface between hole extraction layer and perovskite involves an additional resistance observed at IF. Here, as initially deduced from the photovoltaic performance (Fig. 4c), the solar cell with 0.02G film shows an improvement in J_{SC} and V_{OC}, one order of magnitude lower was the values observed for the device with 0.01G film.

Finally, IS was measured again after a week and, using the same equivalent circuit model, capacitances and resistances were calculated. It is interesting to note that resistances (see Fig. S10) and capacitances (see Fig. S11) extracted at high and low frequency ranges for aged solar cells remain close to the parameters calculated for fresh solar cells. However, the interface between absorber and HTL is altered by graphene concentration in aged solar cells as evidenced in the intermediate frequency regime. Under specific conditions, for slight doping level such as 0.01 mg/mL of graphene, the aged solar cell reduces almost one order of magnitude the capacitance defined at interface between perovskite/HTL (Fig. 7a), while it remains unaltered for aged undoped-PEDOT:PSS perovskite solar cell. This effect was corroborated by the photovoltaic performance (Fig. S12). The 0.01G aged-devices showed better photovoltaic parameters compared to the undoped solar cells. This fact widens the interest of graphene doping the HTL PEDOT:PSS: a small amount of graphene reduces drastically charge accumulation at the interface in aged devices. For higher graphene concentrations (0.015G and 0.02G), the capacitance remains constant after few days under dark conditions (see Fig. S13a and S13b). Similarly, the charge extraction resistance fitted at intermediate frequency shows significant improvements after a week (Fig. 7b) at interface between absorber and 0.01G-doped PEDOT:PSS. This effect is less pronounced for undoped (Fig. 7b),0.015G-doped (Fig. S13c) and 0.02G-doped (Fig. S13d) solar cells.

4. Conclusions

In conclusion, we have successfully developed a facile synthesis method to stabilize and enhance electrical and optical properties adding graphene flakes dispersed into the solution to the widely used polymer
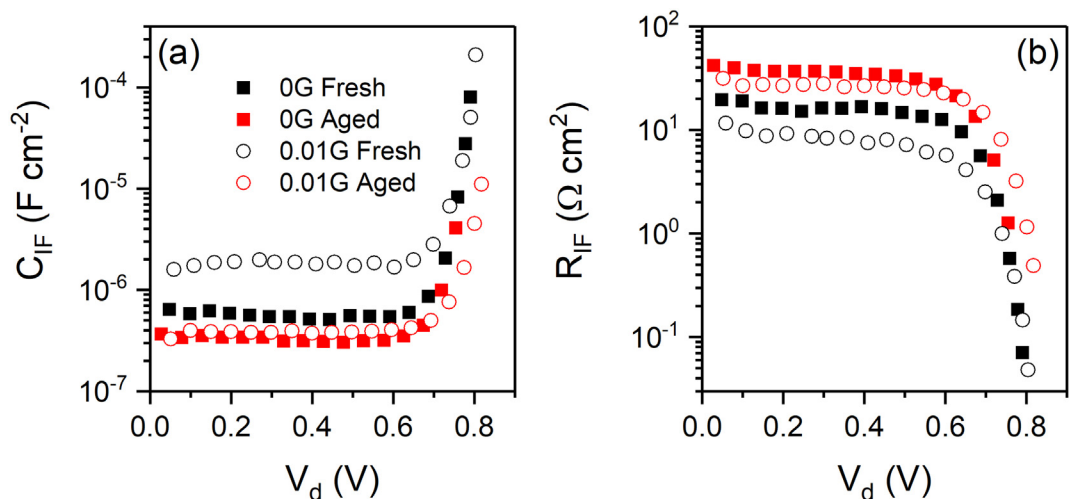

Fig. 7. Capacitance and resistance at IF for fresh (black) and aged (red) perovskite solar cells undoped PEDOT:PSS (square) and 0.01G-doped PEDOT:PSS (circle).

PEDOT:PSS as HTL in inverted perovskite solar cells. Due to this addition, not only PEDOT:PSS layer improves its conductivity, but also the absorber layer deposited on the doped-PEDOT:PSS surface is affected, by increasing the perovskite crystallite sizes and reducing the PbI_2 contribution initially and over time. All photovoltaic parameters are better performed with small graphene content due to an enhancement of charge extraction and a reduction of charge accumulation at the graphene-doped PEDOT:PSS/MAPbI$_3$ interface. This strategy reduces the undesirable reactions from PEDOT:PSS, hygroscopic and acid character of PSS$^-$ group, with the incorporation of graphene and leads to a successful candidate to synthetize effective HTL to be considered in optoelectronic devices.

CRediT authorship contribution statement

C. Redondo-Obispo: Data curation, Formal analysis.**T.S. Ripolles:** Data curation, Writing - review & editing.**S. Cortijo-Campos:** Formal analysis.**A.L. Álvarez:** Funding acquisition, Investigation.**E. Climent-Pascual:** Funding acquisition, Investigation.**A. de Andrés:** Data curation, Writing - review & editing.**C. Coya:** Data curation, Writing - review & editing, Supervision.

Declaration of competing interest

The authors declare that they have no known competing financial interests or personal relationships that could have appeared to influence the work reported in this paper.

Acknowledgement

Appendix A. Supplementary data

Supplementary data to this article can be found online at https://doi.org/10.1016/j.matdes.2020.108587.

References

[1] B.r.-c.e.c.a.J. See https://www.nrel.gov/pv/cell-efficiency.html for NREL. https://www.nrel.gov/pv/cell-efficiency.html.
[2] A.K. Jena, A. Kulkarni, T. Miyasaka, Halide perovskite photovoltaics: background, status, and future prospects, Chem. Rev. 119 (5) (2019) 3036–3103.
[3] X. Tong, F. Lin, J. Wu, Z.M. Wang, High performance perovskite solar cells, Advanced Science 3 (5) (2016), 1500201.
[4] J.S. Shaikh, N.S. Shaikh, A.D. Sheikh, S.S. Mali, A.J. Kale, P. Kanjanaboos, C.K. Hong, J.H. Kim, P.S. Patil, Perovskite solar cells: in pursuit of efficiency and stability, Mater. Des. 136 (2017) 54–80.
[5] E. Climent-Pascual, B.C. Hames, J.S. Moreno-Ramírez, A.L. Álvarez, E.J. Juarez-Perez, E. Mas-Marza, I. Mora-Seró, A. de Andrés, C. Coya, Influence of the substrate on the bulk properties of hybrid lead halide perovskite films, J. Mater. Chem. A 4 (46) (2016) 18153–18163.
[6] P. Schulz, D. Cahen, A. Kahn, Halide Perovskites: is it all about the interfaces? Chem. Rev. 119 (5) (2019) 3349–3417.
[7] J. Luo, J. Xia, H. Yang, L. Chen, Z. Wan, F. Han, H.A. Malik, X. Zhu, C. Jia, Toward high-efficiency, hysteresis-less, stable perovskite solar cells: unusual doping of a hole-transporting material using a fluorine-containing hydrophobic Lewis acid, Energy Environ. Sci. 11 (8) (2018) 2035–2045.
[8] J. You, Z. Hong, Y. Yang, Q. Chen, M. Cai, T.-B. Song, C.-C. Chen, S. Lu, Y. Liu, H. Zhou, Y. Yang, Low-temperature solution-processed perovskite solar cells with high efficiency and flexibility, ACS Nano 8 (2) (2014) 1674–1680.
[9] P. Docampo, J.M. Ball, M. Darwich, G.E. Eperon, H.J. Snaith, Efficient organometal trihalide perovskite planar-heterojunction solar cells on flexible polymer substrates, Nat. Commun. 4 (1) (2013) 2761.
[10] Y. Meng, Z. Hu, N. Ai, Z. Jiang, J. Wang, J. Peng, Y. Cao, Improving the stability of bulk heterojunction solar cells by incorporating pH-neutral PEDOT:PSS as the hole transport layer, ACS Appl. Mater. Interfaces 6 (7) (2014) 5122–5129.
[11] C. Bracher, B.G. Freestone, D.K. Mohamad, J.A. Smith, D.G. Lidzey, Degradation of inverted architecture CH3NH3PbI3-xClx perovskite solar cells due to trapped moisture, Energy Science & Engineering 6 (1) (2018) 35–46.
[12] H.J. Park, H. Kim, J.Y. Lee, T. Lee, L.J. Guo, Optimization of polymer photovoltaic cells with bulk heterojunction layers hundreds of nanometers thick: modifying the morphology and cathode interface, Energy Environ. Sci. 6 (7) (2013) 2203–2210.
[13] U. Würfel, D. Neher, A. Spies, S. Albrecht, Impact of charge transport on current–voltage characteristics and power-conversion efficiency of organic solar cells, Nat. Commun. 6 (1) (2015) 6951.
[14] S.-I. Na, S.-S. Kim, J. Jo, D.-Y. Kim, Efficient and flexible ITO-free organic solar cells using highly conductive polymer anodes, Adv. Mater. 20 (21) (2008) 4061–4067.
[15] A.M. Nardes, R.A.J. Janssen, M. Kemerink, A morphological model for the solvent-enhanced conductivity of PEDOT:PSS thin films, Adv. Funct. Mater. 18 (6) (2008) 865–871.
[16] D. Huang, T. Goh, J. Kong, Y. Zheng, S. Zhao, Z. Xu, A.D. Taylor, Perovskite solar cells with a DMSO-treated PEDOT:PSS hole transport layer exhibit higher photovoltaic performance and enhanced durability, Nanoscale 9 (12) (2017) 4236–4243.
[17] W.E.I. Sha, H. Zhang, Z.S. Wang, H.L. Zhu, X. Ren, F. Lin, A.K.-Y. Jen, W.C.H. Choy, Quantifying efficiency loss of perovskite solar cells by a modified detailed balance model, Adv. Energy Mater. 8 (8) (2018), 1701586.
[18] K. Chen, Q. Hu, T. Liu, L. Zhao, D. Luo, J. Wu, Y. Zhang, W. Zhang, F. Liu, T.P. Russell, R. Zhu, Q. Gong, Charge-carrier balance for highly efficient inverted planar heterojunction perovskite solar cells, Adv. Mater. 28 (48) (2016) 10718–10724.
[19] C. Fei, B. Li, R. Zhang, H. Fu, J. Tian, G. Cao, Highly efficient and stable perovskite solar cells based on monolithically grained CH3NH3PbI3 film, Adv. Energy Mater. 7 (9) (2017), 1602017.
[20] C. Petridis, G. Kakavelakis, E. Kymakis, Renaissance of graphene-related materials in photovoltaics due to the emergence of metal halide perovskite solar cells, Energy Environ. Sci. 11 (5) (2018) 1030–1061.
[21] A. Agresti, S. Pescetelli, B. Taheri, A.E. Del Rio Castillo, L. Cinà, F. Bonaccorso, A. Di Carlo, Graphene–perovskite solar cells exceed 18% efficiency: a stability study, ChemSusChem 9 (18) (2016) 2609–2619.
[22] Z. Liu, S.P. Lau, F. Yan, Functionalized graphene and other two-dimensional materials for photovoltaic devices: device design and processing, Chem. Soc. Rev. 44 (15) (2015) 5638–5679.
[23] M. Acik, S.B. Darling, Graphene in perovskite solar cells: device design, characterization and implementation, J. Mater. Chem. A 4 (17) (2016) 6185–6235.
[24] J.C. Yu, J.A. Hong, E.D. Jung, D.B. Kim, S.-M. Baek, S. Lee, S. Cho, S.S. Park, K.J. Choi, M.H. Song, Highly efficient and stable inverted perovskite solar cell employing PEDOT:GO composite layer as a hole transport layer, Sci. Rep. 8 (1) (2018) 1070.
[25] M. Zhu, W. Liu, W. Ke, L. Xie, P. Dong, F. Hao, Graphene-modified tin dioxide for efficient planar perovskite solar cells with enhanced electron extraction and reduced hysteresis, ACS Appl. Mater. Interfaces 11 (1) (2019) 666–673.
[26] D.-Y. Lee, S.-I. Na, S.-S. Kim, Graphene oxide/PEDOT:PSS composite hole transport layer for efficient and stable planar heterojunction perovskite solar cells, Nanoscale 8 (3) (2016) 1513–1522.
[27] C. Petridis, Y.-H. Lin, K. Savva, G. Eda, E. Kymakis, T.D. Anthopoulos, E. Stratakis, Post-fabrication, in situ laser reduction of graphene oxide devices, Appl. Phys. Lett. 102 (9) (2013), 093115.
[28] X. Huang, H. Guo, J. Yang, K. Wang, X. Niu, X. Liu, Moderately reduced graphene oxide/PEDOT:PSS as hole transport layer to fabricate efficient perovskite hybrid solar cells, Org. Electron. 39 (2016) 288–295.
[29] S. Javaid, C.W. Myung, S. Pourasad, B. Rakshit, K.S. Kim, G. Lee, A highly hydrophobic fluorographene-based system as an interlayer for electron transport in organic–inorganic perovskite solar cells, J. Mater. Chem. A 6 (38) (2018) 18635–18640.
[30] F. Schwierz, Graphene transistors, Nat. Nanotechnol. 5 (2010) 487–496.
[31] L Liu, S. Ryu, M.R. Tomasik, E. Stolyarova, N. Jung, M.S. Hybertsen, M.L. Steigerwald, L.E. Brus, G.W. Flynn, Graphene oxidation: thickness-dependent etching and strong chemical doping, Nano Lett. 8 (7) (2008) 1965–1970.
[32] Q. Chen, F. Zabihi, M. Eslamian, Improved functionality of PEDOT:PSS thin films via graphene doping, fabricated by ultrasonic substrate vibration-assisted spray coating, Synth. Met. 222 (2016) 309–317.
[33] H. Choi, H. Kim, S. Hwang, W. Choi, M. Jeon, Dye-sensitized solar cells using graphene-based carbon nano composite as counter electrode, Sol. Energy Mater. Sol. Cells 95 (1) (2011) 323–325.
[34] J.C. Kim, M.M. Rahman, M.J. Ju, J.-J. Lee, Highly conductive and stable graphene/PEDOT:PSS composite as a metal free cathode for organic dye-sensitized solar cells, RSC Adv. 8 (34) (2018) 19058–19066.
[35] C.-P. Lee, K.-Y. Lai, C.-A. Lin, C.-T. Li, K.-C. Ho, C.-I. Wu, S.-P. Lau, J.-H. He, A paper-based electrode using a graphene dot/PEDOT:PSS composite for flexible solar cells, Nano Energy 36 (2017) 260–267.
[36] T.-H. Han, S.-H. Jeong, Y. Lee, H.-K. Seo, S.-J. Kwon, M.-H. Park, T.-W. Lee, Flexible transparent electrodes for organic light-emitting diodes, 16 (2) (2017) 71–84.
[37] D.H. Yoon, S.H. Yoon, K.-S. Ryu, Y.J. Park, PEDOT:PSS as multi-functional composite material for enhanced Li-air-battery air electrodes, Sci. Rep. 6 (2016), 19962.
[38] P. Kshirsagar, S. Dickreuter, M. Mierzejewski, C.J. Burkhardt, T. Chassé, M. Fleischer, P.D. Jones, Transparent Graphene/PEDOT:PSS microelectrodes for electro- and optophysiology, Advanced Materials Technologies 4 (1) (2019), 1800318.

[39] A.E. Del Rio-Castillo, C. Merino, E. Díez-Barra, E. Vázquez, Selective suspension of single layer graphene mechanochemically exfoliated from carbon nanofibres, Nano Res. 7 (7) (2014) 963–972.

[40] X. Díez-Betriu, S. Álvarez-García, C. Botas, P. Álvarez, J. Sánchez-Marcos, C. Prieto, R. Menéndez, A. de Andrés, Raman spectroscopy for the study of reduction mechanisms and optimization of conductivity in graphene oxide thin films, J. Mater. Chem. C 1 (41) (2013) 6905–6912.

[41] J. Burschka, N. Pellet, S.-J. Moon, R. Humphry-Baker, P. Gao, M.K. Nazeeruddin, M. Grätzel, Sequential deposition as a route to high-performance perovskite-sensitized solar cells, Nature 499 (2013) 316.

[42] X. Huang, K. Wang, C. Yi, T. Meng, X. Gong, Efficient Perovskite hybrid solar cells by highly electrical conductive PEDOT:PSS hole transport layer, Adv. Energy Mater. 6 (3) (2016), 1501773.

[43] C.C. Stoumpos, C.D. Malliakas, M.G. Kanatzidis, Semiconducting tin and Lead iodide perovskites with organic cations: phase transitions, high mobilities, and near-infrared photoluminescent properties, Inorg. Chem. 52 (15) (2013) 9019–9038.

[44] X. Dong, X. Fang, M. Lv, B. Lin, S. Zhang, J. Ding, N. Yuan, Improvement of the humidity stability of organic–inorganic perovskite solar cells using ultrathin Al2O3 layers prepared by atomic layer deposition, J. Mater. Chem. A 3 (10) (2015) 5360–5367.

[45] M. Shirayama, H. Kadowaki, T. Miyadera, T. Sugita, M. Tamakoshi, M. Kato, T. Fujiseki, D. Murata, S. Hara, T.N. Murakami, S. Fujimoto, M. Chikamatsu, H. Fujiwara, Optical transitions in hybrid perovskite solar cells: ellipsometry, density functional theory, and quantum efficiency analyses for $CH_3NH_3PbI_3$, Physical Review Applied 5 (1) (2016), 014012.

[46] J. Bartolomé, E. Climent-Pascual, C. Redondo-Obispo, C. Zaldo, Á. Álvarez, A. de Andrés, C. Coya, Huge photostability enhancement in bismuth-doped methylammonium lead iodide hybrid perovskites by light-induced transformation, Chem. Mater. 31 (10) (2019) 3662–3671.

[47] C. Coya, C. Ruiz, Á. Álvarez, S. Álvarez-García, E.M. García-Frutos, B. Gómez-Lor, A. de Andrés, Star-shaped hexaaryltriindoles small molecules: tuning molecular properties towards solution processed organic light emitting devices, Org. Electron. 13 (10) (2012) 2138–2148.

[48] A.M.A. Leguy, P. Azarhoosh, M.I. Alonso, M. Campoy-Quiles, O.J. Weber, J. Yao, D. Bryant, M.T. Weller, J. Nelson, A. Walsh, M. van Schilfgaarde, P.R.F. Barnes, Experimental and theoretical optical properties of methylammonium lead halide perovskites, Nanoscale 8 (12) (2016) 6317–6327.

[49] J.I. Pankove, Optical Processes in Semiconductors, Dover, New York, 1971.

[50] S. De Wolf, J. Holovsky, S.-J. Moon, P. Löper, B. Niesen, M. Ledinsky, F.-J. Haug, J.-H. Yum, C. Ballif, Organometallic halide perovskites: sharp optical absorption edge and its relation to photovoltaic performance, J. Phys. Chem. Lett. 5 (6) (2014) 1035–1039.

[51] W. Nie, J.-C. Blancon, A.J. Neukirch, K. Appavoo, H. Tsai, M. Chhowalla, M.A. Alam, M.Y. Sfeir, C. Katan, J. Even, S. Tretiak, J.J. Crochet, G. Gupta, A.D. Mohite, Light-activated photocurrent degradation and self-healing in perovskite solar cells, Nat. Commun. 7 (2016), 11574.

[52] A. Szemjonov, K. Galkowski, M. Anaya, Z. Andaji-Garmaroudi, T.K. Baikie, S. Mackowski, I.D. Baikie, S.D. Stranks, M.S. Islam, Impact of oxygen on the electronic structure of triple-cation halide perovskites, ACS Materials Letters 1 (5) (2019) 506–510.

[53] N.D. Pham, V.T. Tiong, P. Chen, L. Wang, G.J. Wilson, J. Bell, H. Wang, Enhanced perovskite electronic properties via a modified lead(ii) chloride Lewis acid–base adduct and their effect in high-efficiency perovskite solar cells, J. Mater. Chem. A 5 (10) (2017) 5195–5203.

[54] C. Wang, H. Hao, S. Chen, K. Cao, H. Yu, Q. Zhang, G. Wan, W. Shang, W. Huang, Inverse-architecture perovskite solar cells with 5,6,11,12-tetraphenylnaphthacene as a hole conductor, RSC Adv. 7 (48) (2017) 29944–29952.

[55] M.A. Mahmud, N.K. Elumalai, M.B. Upama, D. Wang, B. Puthen-Veettil, F. Haque, M. Wright, C. Xu, A. Pivrikas, A. Uddin, Controlled Ostwald ripening mediated grain growth for smooth perovskite morphology and enhanced device performance, Sol. Energy Mater. Sol. Cells 167 (2017) 87–101.

[56] D. Liu, Y. Li, J. Yuan, Q. Hong, G. Shi, D. Yuan, J. Wei, C. Huang, J. Tang, M.-K. Fung, Improved performance of inverted planar perovskite solar cells with F4-TCNQ doped PEDOT:PSS hole transport layers, J. Mater. Chem. A 5 (12) (2017) 5701–5708.

[57] F. Fabregat-Santiago, G. Garcia-Belmonte, I. Mora-Seró, J. Bisquert, Characterization of nanostructured hybrid and organic solar cells by impedance spectroscopy, Phys. Chem. Chem. Phys. 13 (20) (2011) 9083–9118.

[58] A.R. Kumar, M.S. Suresh, J. Nagaraju, Measurement of AC parameters of gallium arsenide (GaAs/Ge) solar cell by impedance spectroscopy, IEEE Transactions On Electron Devices 48 (9) (2001) 2177–2179.

[59] E. Guillén, F.J. Ramos, J.A. Anta, S. Ahmad, Elucidating transport-recombination mechanisms in perovskite solar cells by small-perturbation techniques, J. Phys. Chem. C 118 (40) (2014) 22913–22922.

[60] J.-P. Correa-Baena, S.-H. Turren-Cruz, W. Tress, A. Hagfeldt, C. Aranda, L. Shooshtari, J. Bisquert, A. Guerrero, Changes from bulk to surface recombination mechanisms between pristine and cycled perovskite solar cells, ACS Energy Lett. 2 (3) (2017) 681–688.

[61] L. Contreras-Bernal, M. Salado, A. Todinova, L. Calio, S. Ahmad, J. Idígoras, J.A. Anta, Origin and whereabouts of recombination in perovskite solar cells, J. Phys. Chem. C 121 (18) (2017) 9705–9713.

[62] L. Contreras-Bernal, S. Ramos-Terrón, A. Riquelme, P.P. Boix, J. Idígoras, I. Mora-Seró, J.A. Anta, Impedance analysis of perovskite solar cells: a case study, J. Mater. Chem. A 7 (19) (2019) 12191–12200.

[63] S.-M. Yoo, S.J. Yoon, J.A. Anta, H.J. Lee, P.P. Boix, I. Mora-Seró, An equivalent circuit for perovskite solar cell bridging sensitized to thin film architectures, Joule 3 (10) (2019) 2535–2549.

[64] A. Todinova, L. Contreras-Bernal, M. Salado, S. Ahmad, N. Morillo, J. Idígoras, J.A. Anta, Towards a universal approach for the analysis of impedance spectra of perovskite solar cells: equivalent circuits and empirical analysis, ChemElectroChem 4 (11) (2017) 2891–2901.

[65] A. Guerrero, G. Garcia-Belmonte, I. Mora-Sero, J. Bisquert, Y.S. Kang, T.J. Jacobsson, J.-P. Correa-Baena, A. Hagfeldt, Properties of contact and bulk impedances in hybrid Lead halide perovskite solar cells including inductive loop elements, J. Phys. Chem. C 120 (15) (2016) 8023–8032.